INTERNATIONAL JOURNAL FOR NUMERICAL AND ANALYTICAL METHODS IN GEOMECHANICS
Int. J. Numer. Anal. Meth. Geomech. 2017; **41**:627–653
Published online 18 September 2016 in Wiley Online Library (wileyonlinelibrary.com). DOI: 10.1002/nag.2557

A fully coupled method for massively parallel simulation of hydraulically driven fractures in 3-dimensions

Randolph R. Settgast*,†, Pengcheng Fu, Stuart D. C. Walsh,
Joshua A. White, Chandrasekhar Annavarapu and Frederick J. Ryerson

Lawrence Livermore National Laboratory, Livermore, CA 94550, U.S.A.

SUMMARY

This paper describes a fully coupled finite element/finite volume approach for simulating field-scale hydraulically driven fractures in three dimensions, using massively parallel computing platforms. The proposed method is capable of capturing realistic representations of local heterogeneities, layering and natural fracture networks in a reservoir. A detailed description of the numerical implementation is provided, along with numerical studies comparing the model with both analytical solutions and experimental results. The results demonstrate the effectiveness of the proposed method for modeling large-scale problems involving hydraulically driven fractures in three dimensions. © 2016 The Authors. International Journal for Numerical and Analytical Methods in Geomechanics published by John Wiley & Sons Ltd.

Received 4 March 2016; Revised 7 May 2016; Accepted 27 June 2016

KEY WORDS: hydraulic fracture; fracture mechanics; geomechanics; high-performance computing

1. INTRODUCTION

Hydraulic fracturing used in combination with horizontal drilling has driven the growth in oil and gas production in the continental USA over the last decade. The application of these technologies has resulted in dramatic increases in oil production from shale oil to co-produced gas [1], fundamentally altering the global energy landscape. However, there remains ample opportunity for increases in reservoir efficiency through improved completion design, as well as reducing the environmental impacts of recovery operations. Specifically, increasing the total hydrocarbon recovered over the lifetime of a reservoir, and mitigating the rapid decline in production experienced by many wells [2] would provide cost reductions that would improve the economic viability of shale reservoirs. A detailed understanding of the underlying physics governing hydraulic fracturing processes is necessary to make informed engineering decisions that enhance reservoir productivity. However, given the economic constraints, detailed experimental investigations – particularly at the field-scale – are not always feasible. Consequently, most of the current understanding of the hydraulic fracturing process stems from empirical observations or simplified models. Rigorous numerical methods capable of simulating the many coupled processes involved in hydraulic fracturing in arbitrary three-dimensional geometries are necessary to develop guidelines for best practices and devise new strategies to improve well performance; such numerical models and methods should have sufficient capability to model the inherently heterogeneous subsurface environment present in real-world problems.

*Correspondence to: R. R. Settgast, Lawrence Livermore National Laboratory, Livermore, CA 94550, U.S.A.
†E-mail: rrsettgast@gmail.com

A historical overview of the hydraulic fracturing technology and an account of some of the early numerical models can be found in Adachi *et al.* [3]. Notably, Boone and Ingraffea [4] first presented a procedure consisting of a finite element model of a two-dimensional poro-elastic medium coupled with a finite difference scheme for modeling fluid flow along a fracture. Several subsequent attempts have also been made to model hydraulic fracturing with zero-thickness interface elements. Most notably, Secchi *et al.* [5, 6] presented a cohesive fracture model in a fully saturated porous medium in both two and three dimensions. In recent years, generalized and extended finite element methods (XFEM) have also been applied to this class of problems. Mohammadnejad and Khoei [7] described an XFEM approach for a cohesive crack model in a deformable porous medium. Khoei *et al.* [8] presented an XFEM approach for modeling hydraulically driven cohesive fracture propagation in the presence of frictional natural faults. Irzal *et al.* [9] discussed modeling fluid flow through a progressively fracturing porous medium subject to large deformations within an XFEM framework. It must be noted that the aforementioned studies were limited to two-dimensional models. More recently, Gupta and Duarte [10] presented a GFEM approach to model three-dimensional non-planar hydraulic fracture propagation.

In this work, we present a fully coupled finite element/finite volume approach for modeling hydraulically driven fractures with arbitrary three-dimensional geometries. The proposed approach facilitates a realistic representation of local heterogeneities, layering and natural fracture networks in a reservoir, and moreover allows for spontaneous fracture nucleation. In the method proposed here, fractures are restricted to lie on inter-element boundaries. However, this restriction does not prevent the re-positioning of those faces via mesh relaxation as described by [11]. Our approach is closest in implementation to a cohesive interface element approach with an extrinsic traction separation law, as we adaptively split the finite element faces once a specified failure criterion is met.

In this paper, particular emphasis is placed on the algorithmic details necessary to adapt the fully coupled finite element/finite volume approach to model large-scale problems on massively paralleled high-performance computing platforms. The algorithmic details pertaining to adaptive modification of mesh-topology are also discussed. While several numerical studies for modeling hydraulic fracturing exist, to our knowledge, the approach presented here is the first to address field scale three-dimensional problems on massively parallel computing platforms.

The proposed method is implemented in GEOS: a flexible multi-scale, multi-physics simulation environment developed at Lawrence Livermore National Laboratory. GEOS's current capabilities include simulation of hydraulic fracture stimulation in two and three dimensions [12–14]; induced micro-seismicity [15]; modeling geochemical transport and reaction [16, 17]; geothermic drawdown-[18, 19]; and simulations of immiscible fluid flow [20]. Although a versatile platform designed for a range of geological applications, to date the development of the GEOS software platform has been primarily targeted towards characterizing oil and gas reservoir behavior in response to fluid-induced perturbations, including different stimulation and fracture control techniques and hydraulic stimulation of enhanced geothermal systems.

In what follows, we first describe the governing equations for modeling the coupled process of hydraulic fracturing (Section 2) and then present the discretized forms of the governing equations (Section 3). We further discuss the technique used to simulate fracture extension on the coarse mesh sizes applicable to field scale problems, as well as a specific method for altering mesh topology in a distributed memory environment (Section 4). We then validate the proposed approach by comparing several benchmark numerical examples with existing analytical and experimental studies (Sections 5 and 5.2). Field-scale numerical investigations demonstrating the utility of the proposed approach in guiding real-engineering decisions are also provided (Section 5.3).

2. GOVERNING EQUATIONS

Under the method proposed in this paper, hydraulic fracture propagation is modeled as a multi-physics problem in which solutions for both the deformation of the solid continuum and the flow along the fractured interface are solved simultaneously. The response of the solid body is modeled using the finite element method, while the fluid flow within the fracture is modeled using a finite-volume method that applies lubrication theory to reduce the dimensionality of the flow problem to

DOI: 10.1002/nag

a 2-dimensional surface. The two methods are naturally coupled, with the fluid pressure applied to the surface of the fracture, and the solid deformation defining the the aperture height/storage volume of the fracture. Fracture propagation is governed by applying energy-based fracture mechanics concepts to the discretized mesh. This approach yields a robust method that scales well to large numbers of processors and accurately captures the pertinent physics for these classes of problems. A concrete definition of the proposed formulation is provided in the succeeding text.

2.1. *Strong formulation*

Consider a body Ω with external boundaries Γ_t and Γ_d, where traction and kinematic boundary conditions are applied, respectively (Figure 1). Γ_c denotes an internal boundary to the body and represents the initially coincident fracture surfaces, which may evolve in response to stresses acting on the body. The governing equations for the quasi-static solid deformation of body Ω are given as follows:

$$\begin{aligned} T_{ij,j} &= b_i && \text{in } \Omega, \\ u_i &= u_i^{\mathrm{d}} && \text{on } \Gamma_{\mathrm{d}}, \\ T_{ij} n_j &= t_i && \text{on } \Gamma_{\mathrm{t}}, \\ T_{ij}(n_c^+)_j &= -T_{ij}(n_c^-)_j = -p(n_c^+)_i + c_i^+ + f_i^{c+} && \text{on } \Gamma_{\mathrm{c}}, \end{aligned} \tag{1}$$

where T_{ij} is the Cauchy stress tensor, b_i is the body force (e.g., gravity), u_i is the displacement vector, t_i is the externally applied traction, n_i is the outward normal to the external surface, n_c is the outward normal to the crack surface, p is the fluid pressure in the fracture, c_i is the cohesive traction, and f_i^c is the contact force. Note that in fluid driven stimulation of oil/gas reservoirs, fractures propagate at rates much less than the Rayleigh wave speed. Therefore, it is reasonable to neglect the inertial terms in the equations of motion and use static equilibrium defined in Equation (1).

Flow of fluid in the fracture is assumed to follow classic lubrication theory, which allows for the fluid flow problem to be reduced to a two-dimensional problem in the plane of the fracture (Γ_c). The equations of mass and momentum conservation lead to the Reynolds equation of classical lubrication theory:

$$\tfrac{\partial}{\partial t}(\rho w) - \tfrac{1}{12\mu}\nabla \cdot \rho(w^3 \nabla p) = 0, \tag{2}$$

where μ is the dynamic viscosity of the fluid, p is the fluid pressure, w is the fracture aperture $w = [\![\mathbf{u}]\!] \cdot \mathbf{n}$, and ρ is the fluid density. The jump in the displacement across the fracture surface is denoted by $[\![\mathbf{u}]\!]$.

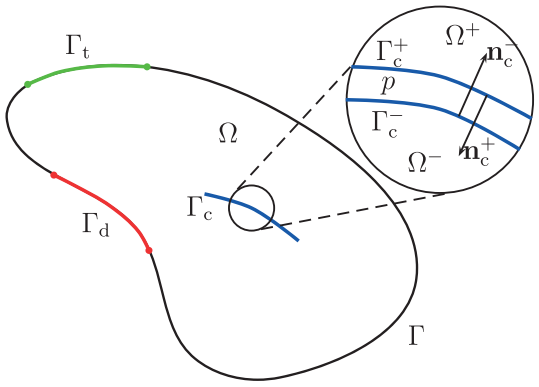

Figure 1. Notation for the model problem. Assume that there is a continuous domain Ω, with the Dirichlet boundary specified by Γ_d and the Neumann boundary specified by Γ_t. Γ_c^+ and Γ_c^- represent the initially coincident fracture faces, which are subjected to applied cohesive tractions $\mathbf{c}$, fluid pressures p, as well as contact constraints. [Colour figure can be viewed at wileyonlinelibrary.com]

DOI: 10.1002/nag

The evolution of the fluid pressure (p) and its relation with the volume represented within Γ_c form the basis of the coupling between the deformation problem defined by Equation (1) and the fluid flow problem defined by Equation (2).

3. DISCRETIZATION

3.1. Solid deformation

The governing equations for the solid body are approximated with the standard Galerkin finite element method. Integration over the elements that comprise the discretized body yields an expression for the element contributions to solid body residual as

$$\left(R^e_{solid}\right)_{ai} = \int_{\Gamma^e_t} \Phi_a t_i \, dA + \int_{\Gamma_c} \Phi_a \left(f^c_i + c_i - p n_i\right) dA - \int_{\Omega^e} \Phi_{a,j} T_{ij} dV + \int_{\Omega^e} \Phi_a \rho_m b_i \, dV, \quad (3)$$

where a is a nodal index, i is the spatial direction, Φ is the finite element shape functions, and ρ_m is density of the matrix material. A simple linear penalty contact law is enforced on Γ_c such that

$$f^c_i = k[\![x]\!]_j n_j n_i, \quad (4)$$

where $[\![x]\!]$ signifies the jump in displacement across Γ_c, and k is the contact stiffness.

3.2. Fluid flow along the fracture

The flow problem described by Equation (2) is discretized using a finite volume method. The dimensions of the individual finite volumes (V_r, where r is the index over all finite volumes on Γ_c), are defined by the product of the projected area (A_r) and the aperture (w_r) as illustrated in Figure 2. The area (A_r) is the intersection of the projection of a pair of separated faces onto a plane that bisects the line between face centers and has normal equal to the average normal of those faces.

The fluid degrees of freedom (m_f for fluid mass, or p for fluid pressure) are represented as cell centered quantities stored on V_r. The discretized governing equation takes the form of

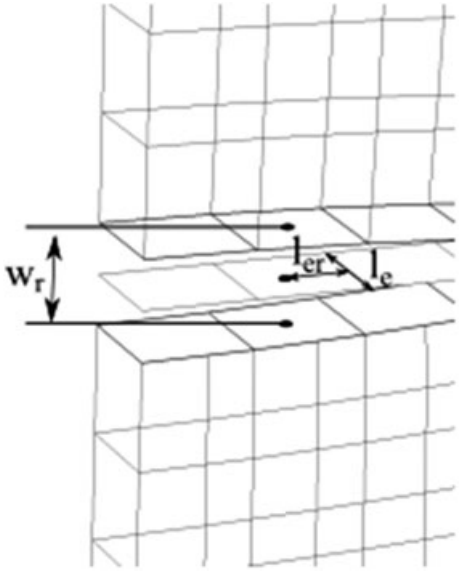

Figure 2. Illustration of defined finite volume for coupled deformation/flow problem.

DOI: 10.1002/nag

$$
\begin{aligned}
(R_{fluid})_r &= \frac{dm_r}{dt} - \sum_{e \in r} \bar{\rho}_{er} \kappa_{er} (p_e - p_r) - q_r^{in} \\
&= \frac{d\,(\rho_r V_r)}{dt} - \sum_{e \in r} \bar{\rho}_{er} \kappa_{er} (p_e - p_r) - q_r^{in}, \text{where}
\end{aligned}
\tag{5}
$$

$$
\kappa_{er} = \frac{w_r^3 l_e}{12 \mu l_{er}}. \tag{6}
$$

In Equation (5), p_r is the fluid pressure on face r, p_e is the fluid pressure on edge e, $\bar{\rho}_{er}$ is the density of the fluxed volume into the cell from edge (e), and q_r^{in} is a source/sink term. In the context of hydraulic fracture simulations, the sink/source term would typically correspond to fluid injection at the wellbore (source), and fluid leak-off from the surface of the fracture Γ_c into the surrounding continuum. In Equation (6), the quantity l_{er} is the distance from center of face r to the center of edge e, and l_e is the effective cross-section for flow across edge e.

The preceding fluid equations define a relation for conservation of mass for a single-finite volume, with the summation of all fluxes from all attached edges into/out of the volume that relies on knowledge of the unknown fluid pressure at the edge (p_e). To determine the pressure on an edge (p_e) in terms of the known quantities and the specified degrees of freedom, conservation of mass flow is applied to the edge which gives an expression for the pressure at edge e as

$$
p_e = \frac{\sum_{r \in e} \bar{\rho}_{er} \kappa_{er} p_r}{\sum_{r \in e} \bar{\rho}_{er} \kappa_{er}} \approx \frac{\sum_{r \in e} \kappa_{er} p_r}{\sum_{r \in e} \kappa_{er}}, \tag{7}
$$

where we have simplified the expression by assuming constant density flowing through the edge, thus removing density from the expression. Because the density of the fluid does not vary greatly, the assumption of constant density introduces minimal errors for cases where there are more than two faces connected to a single edge. In the case of a highly compressible fluid, the effects of this assumption along with the effects of additional frictional losses due to the geometry of the intersection would require a more rigorous treatment.

One feature of hydraulically driven fractures in the field is the loss of fluid from the main fracture into a combination of natural fractures and porous rock material, or 'leak-off'. A simple approach to modeling this effect is to model the fluid loss through a sink term in Equation (5). Carter's leak-off method first described in [21] defines a simple sink term as

$$
\Lambda = \frac{2 C_L}{\sqrt{t - t_0}}, \tag{8}
$$

where C_L is the so-called Carter's leak-off coefficient and t_0 is the time when the current flow element was first saturated. In addition to this empirical treatment, GEOS is capable of modeling fluid leak-off from the fracture by treating the rock matrix as a porous medium and/or directly modeling flowing into pre-existing natural fractures.

3.3. Temporal discretization

Advancing a simulation forward in time requires a strategy for satisfying the residuals specified in Equations (3) and (5) over a discrete timestep, which is defined as $\Delta t = t_{n+1} - t_n$. Earlier works have described an approach for the explicit time integration of the governing equations [12], [14]. However, the use of explicit integration requires the use of some undesirable methods such as excessive mass scaling, and the use of very low fluid stiffness in order to achieve a reasonable stable timestep for this class of problem. Here, we focus on the fully implicit time integration of governing Equations (3) and (5), as a fully implicit time integration allows for a stable solution without modification of physical parameters.

DOI: 10.1002/nag

The discrete equations of static equilibrium defined by Equation (3) are enforced at the end of every discrete timestep t^{n+1}. Applying superscripts to denote the location in time, Equation (3) becomes

$$\begin{aligned}\left(R^{e}_{solid}\right)^{n+1}_{ai} = &\int\limits_{\Gamma^e_t} \Phi_a t_i^{n+1} dA - \int\limits_{\Omega^e} \Phi_{a,j}\, T_{ij}^{n+1} dV + \int\limits_{\Omega^e} \Phi_a \rho^{n+1} b_i^{n+1} dV \\ &+ \int\limits_{\Gamma^e_c} \Phi_a \left(\left(f_i^{c+}\right)^{n+1} - p^{n+1} n_i \right) dA.\end{aligned} \tag{9}$$

For the conservation of mass for the fluid in the fracture, a modified backwards Euler method is applied to equation (5) over Δt, which yields

$$\begin{aligned}\left(R_{fluid}\right)^{n+1}_{r} &= \left(\rho_r^{n+1} V_r^{n+1} - \rho_r^n V_r^n\right) - \Delta t \left(\sum_{e \in r} \bar{\rho}_{er}^{n+1} \kappa_{er}^{n+1} \left(p_e^{n+1} - p_r^{n+1}\right) + q_r^{in} \right), \\ &= \left(\rho_r^n \Delta V_r + \Delta \rho_r V_r^n + \Delta V_r \Delta \rho_r\right) \\ &- \Delta t \left(\sum_{e \in r} \bar{\rho}_{er}^{n+1} \kappa_{er}^{n+1} \left(p_e^{n+1} - p_r^{n+1}\right) + q_r^{in} \right),\end{aligned} \tag{10}$$

where

$$\Delta \rho_r = \left. \frac{\partial \rho_r}{\partial p_r} \right|_{\Delta t} \Delta p_r. \tag{11}$$

The residuals for the FEM equations of static equilibrium defined in Equation (9) and the residual defined from conservation of fluid mass in the fracture Equation (10) are combined to form a block structured residual system of equations for fully coupled deformation and flow

$$\left[\mathbf{R}^{n+1}\right] = \left[\begin{array}{c} \mathbf{R}^{n+1}_{solid} \\ \hline \mathbf{R}^{n+1}_{fluid} \end{array} \right] = \left[\mathbf{0} \right]. \tag{12}$$

We refer to Equation (12) as a 'fully coupled system' because of the tight coupling of solid displacements and fluid pressures in Equations (9) and (10). Specifically, in Equation (9), the term for fluid pressure applied to the crack surface provides a mechanism by which the fluid pressure solution influences the displacement solution. In Equation (10), the fluid volume is directly related to the displacements of the nodes on the crack surface, which is the mechanism by which the displacements may influence the pressure solution. In general, Equation (12) describes a non-linear system of equations, with the major non-linearities originating from any contact forces present in Equation (9), the non-linear nature of the permeability defined in Equation (6), and the potentially non-linear relation between fluid density and fluid pressure. Therefore, Equation (12) can be solved using an iterative non-linear method, such as Newton's method, where the iterations are defined by

$$\mathbf{J}\left(\mathbf{y}_k^{n+1}\right)\left(\mathbf{y}_{k+1}^{n+1} - \mathbf{y}_k^{n+1}\right) = -\mathbf{R}\left(\mathbf{y}_k^{n+1}\right), \tag{13}$$

where k is the iteration count, $\mathbf{y}$ is the vector of degrees-of-freedom, and $\mathbf{J}$ is the block structured Jacobian derivative. The degree of freedom vector and the Jacobian matrix are defined as follows:

DOI: 10.1002/nag

$$\mathbf{y} = \left[\frac{\mathbf{u}}{\mathbf{p}}\right] = \left[\frac{u_{ai}}{p_r}\right] = \begin{bmatrix} u_{11} \\ u_{12} \\ u_{13} \\ u_{21} \\ \vdots \\ u_{(nnodes)(nsdof)} \\ \hline p_r^{n+1} \\ \vdots \\ p_{npdof}^{n+1} \end{bmatrix}, \tag{14}$$

$$\mathbf{J}(\mathbf{y}) = \left[\begin{array}{c|c} \frac{\partial \mathbf{R}_{solid}}{\partial \mathbf{u}} & \frac{\partial \mathbf{R}_{solid}}{\partial \mathbf{p}} \\ \hline \frac{\partial \mathbf{R}_{fluid}}{\partial \mathbf{u}} & \frac{\partial \mathbf{R}_{fluid}}{\partial \mathbf{p}} \end{array}\right]\Bigg|_{\mathbf{y}}. \tag{15}$$

The iterative scheme outlined in Equation (13) provides updates to the displacement/pressure degree-of-freedom vector defined in Equation (14) until the residual defined by Equation 12 is satisfied to a desired tolerance. It is important to note that Equation (12) is a block vector involving two quantities with different units, and thus vastly different scales. Because of this discrepancy between the blocks, it may be ineffective to simply use a vector norm of the full block residual defined by Equation (12) and attempt to compare that result with a chosen tolerance. Alternatively, each block in Equation (12) is individually scaled prior to calculation of a vector norm. For the solid residual block given by Equation (3), each residual equation itself represents the sum of all forces acting on a node in each coordinate direction. Therefore, the scaling factor is chosen to be the largest magnitude force in the problem, which is the maximum force contribution to any node in the problem defined by

$$f_{max} = max\left(\int_{\Omega^e} \Phi_{a,j}\, T_{ij}^{n+1} dV\right) \forall e \in \Omega. \tag{16}$$

For the fluid residuals defined by Equation (10), each residual equation represents the mass error for a single-finite volume. Therefore, the largest mass contained in any finite volume in the problem is selected as the normalization factor

$$m_{max} = max\,(m_r)\, \forall r \in \Gamma_c. \tag{17}$$

The application of Equations (16) and (17) to (12) gives

$$[\hat{\mathbf{R}}^{n+1}] = \left[\begin{array}{c} \frac{\mathbf{R}_{solid}^{n+1}}{f_{max}} \\ \hline \frac{\mathbf{R}_{fluid}^{n+1}}{m_{max}} \end{array}\right] = \left[\,\mathbf{0}\,\right], \tag{18}$$

which is a unit-less set of residual equations that are scaled with the maximum quantities present in the problem. In effect, this implies that the norm of Equation (18) may be compared with an absolute tolerance relative to unity. For example, a residual convergence tolerance of 10^{-6} results in a residual that has achieved approximately six digits of precision.

4. MESH TOPOLOGY EVOLUTION AND FRACTURING CRITERION

In this work, the generation of new surfaces in the solid body (i.e., fracture propagation) is restricted to fracture along inter-element faces. In the context of hydraulic fracture simulations, the direction of propagating fractures are typically governed by the stress field in the vicinity of the crack tip.

DOI: 10.1002/nag

The hydraulic fractures are generally inclined to propagate perpendicular to the minimum *it situ* principal stress direction, although features such as nearby hydraulically driven fractures from the same simulation job may re-orient the stress tensor from the *it situ* stress field. Natural fractures are typically modeled by assuming that they form in 'joint sets' consisting of fractures that are essentially parallel. In cases where the *it situ* stresses are significantly anisotropic, it is appropriate to construct a finite element mesh that accommodates these plane orientations to capture the natural and hydraulic fractures most crucial to the application. In cases where the *it situ* stresses are not strongly anisotropic, remeshing and mesh-smoothing techniques provide an option to adequately model fracture orientations. One approach for modeling arbitrary crack paths by remeshing to allow for fracture propagation in the preferential direction is given in [11]. An investigation into the use of mesh relaxation and element splitting via X-FEM to attain truly mesh independent solutions is beyond the scope of the present study. Instead, we focus on the verification and validation of the overall approach to coupling fluid flow and solid mechanics, and modeling field cases that do not require full path independence.

Four key aspects of the proposed method are discussed: (i) a modification to the virtual crack closure technique originally presented in [22] for the calculation of energy release rate; (ii) a mixed-mode rupture criterion that determines the desired trajectory of the fracture: (iii) a node-centered logic for the topological updates required by the creation or extension of fractures; and (iv) special algorithms that enable topology changes in parallel are presented in the sections as follows.

4.1. Calculation of stress intensity factors

In GEOS, a three-dimensional fracture front is represented by a collection of line segments or FEM 'edges'. When evaluating the rupture criterion, Modes-I and II stress intensity factors (K_I, K_{II}) are calculated for each edge based on stress and deformation states of the finite elements surrounding this edge. A discussion of various methods to calculate stress intensity factor in the context of finite element methods is given by [23]. Three-dimensional simulations at reservoir scales require that the method for SIF calculation is robust and reasonably accurate for relatively coarse mesh resolution near the fracture tip (i.e., 1 m). Moreover, it is highly desirable to rely exclusively on the states of elements directly connected to the edge to minimize inter-partition ghosting requirements in distributed memory computing environments. As the simulations presented in this work demonstrate, a modified virtual crack closure technique (MVCCT) satisfies these requirements and provides sufficient accuracy for the problems of interest.

Figure 3 illustrates the two configurations required to describe the calculation of a stress intensity factor for separation of the node '*node a*' using the proposed MVCCT. Note that a 2D geometry is shown to visualize the concepts, and an edge in three-dimensions collapses into a node in 2-dimensions. The focus of Figure 3 is on a single (upper) side of the fracture plane, while the elements on the opposite side of the fracture plane are shown in gray.

The application of fluid pressure corresponding to the 'intact' configuration is shown in Figure 3(a), and Figure 3(c) illustrates the nodal displacements and forces that are relevant for the derivation of the MVCCT. Specifically, the force on *node b* resulting from the integration of the external tractions (e.g., fluid pressure) on the crack surface is shown as $\mathbf{f}^b_{external}$, and the scalar representation of the vector between the *node b* and its sibling node (i.e., $[\![\mathbf{x}_b]\!]$) is given as $\mathbf{w}_b$. The force ($\mathbf{f}_{disconnected}$) is the force on *node a* resulting from the volume integral on the divergence of the stress tensor, as described in Equation (3), from the finite elements on lower side of the fracture plane that have been disconnected from *node a*.

Figure 3(b) shows the application of fluid pressure corresponding to 'virtual fracture' configuration. The 'virtual fracture' configuration illustrates the mesh as if *node a* has been split and is useful for the energy analysis that is the basis for the MVCCT. Figure 3(d) illustrates the relevant nodal displacements and forces in the 'virtual fracture' configuration that is required for the derivation of the MVCCT. Specifically, the force on *node a* resulting from the integration of the external tractions (e.g., fluid pressure) on the crack surface is shown as $\mathbf{f}^a_{external}$, and the scalar representation of the vector between *node a* and its sibling node *node a'* (i.e., $[\![\mathbf{x}_a]\!]$) is given as $\mathbf{w}_a$.

DOI: 10.1002/nag

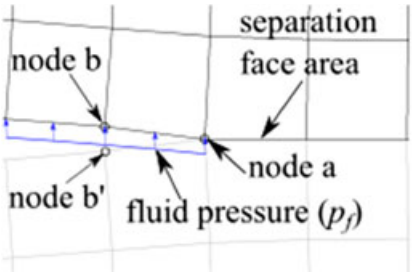

(a) Physical description of "Intact" configuration ($t = t_0$)

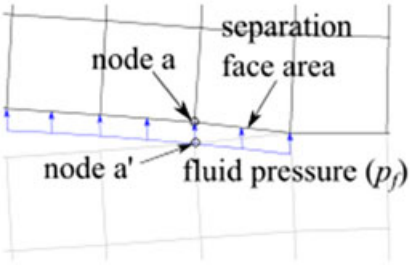

(b) Physical description of "Virtual Fracture" configuration ($t = t_f$)

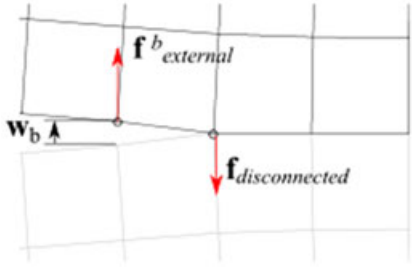

(c) Relevant nodal forces and opening displacements in "Intact" configuration ($t = t_0$)

(d) Relevant nodal forces and opening displacements in "Virtual Fracture" configuration ($t = t_f$)

Figure 3. Mesh configurations with relevant quantities for modified virtual crack closure technique. The upper diagrams define the topology and physical problem, and the lower diagrams define the quantities used for the modified virtual crack closure technique. The focus is on the upper side of the separation plane, with the lower side shown in gray. [Colour figure can be viewed at wileyonlinelibrary.com]

Two assumptions that are required for use of this method is that *node a* attains the configuration of *node b* once *node a* has fractured, and that the displacement of *node a* varies linearly in time:

$$\mathbf{f}^{a}_{external}(t_f) = \mathbf{f}^{b}_{external}(t_0), \tag{19a}$$

$$\mathbf{w}_a(t) = \mathbf{w}_b(t_0)\left(\frac{t - t_0}{t_f - t_0}\right) \text{ from } (t_0 < t < t_f). \tag{19b}$$

The closure force ($\mathbf{f}_{closure}$) represents the force required to *node a* in the 'virtual fracture' configuration (with an equal and opposite force being applied to *node a'*) such that *node a* and *node a'* are coincident as in the initial configuration. The closure force is expressed as a linear-in-time function

$$\mathbf{f}_{closure}(t) = \left(\mathbf{f}_{disconnected} - \mathbf{f}^{b}_{external}(t_0)\right)\left(\frac{t - t_0}{t_f - t_0}\right). \tag{20}$$

The estimate of the energy release rate ($\mathbf{G}$) for splitting *node a* is defined by the work done by both closure forces ($\mathbf{f}_{closure}$ on *node a* and $-\mathbf{f}_{closure}$ on *node a'*) moving a distance of $(1/2\mathbf{w}_a)$ divided by the new surface area generated (A), or

$$\begin{aligned}\mathbf{G} &= -\frac{1}{A}\int_{t_0}^{t_f} \mathbf{f}_{closure}(t) \circ \left(\frac{d\,\mathbf{w}_a(t)}{dt}\right) dt, \\ &= -\frac{1}{2A}\left(\left(\mathbf{f}_{disconnected} - \mathbf{f}^{b}_{external}(t_0)\right)\right) \circ \mathbf{w}_b,\end{aligned} \tag{21}$$

where ($\circ$) is the Hadamard product, or entrywise product. The vector components of $\mathbf{G}$ can be correlated to (G_I, G_{II}, G_{III}) if rotated to the appropriate coordinate system (I-direction normal to the fracture plane, II-direction in the direction of propagation, III-direction in the direction of the fracture front). The scalar value of the energy release rate is the sum of the components of $\mathbf{G}$

DOI: 10.1002/nag

$$G = G_I + G_{II} + G_{III}. \tag{22}$$

The calculated value of the energy release rate is compared with the critical energy release rate, which is typically expressed in terms of the mode I stress intensity factor by the standard relation

$$G_c = K_{Ic}^2 \left(\frac{1 - \nu^2}{E} \right). \tag{23}$$

Finally, the stress intensity factors of each mode are estimated using the standard relations for plane strain fracture:

$$\begin{aligned} K_I &= \sqrt{\left(\frac{E}{1 - \nu^2} \right) G_I}\,, \\ K_{II} &= \sqrt{\left(\frac{E}{1 - \nu^2} \right) G_{II}}\,, \\ K_{III} &= \sqrt{(2\mu)\, G_{III}}. \end{aligned} \tag{24}$$

4.2. Mixed mode rupture criterion

Once the energy release rate, calculated using Equation (21), exceeds the critical value (i.e., $G > G_c$), the fracture is ready to propagate from this edge into the intact solid medium. Because the proposed method restricts the fracture to a path along the inter-element faces connected to this edge, and the mesh is considered fixed (i.e., no global remeshing or smoothing), the rupture criterion is required to determine which face will rupture. To determine which face should be ruptured, we first establish a cylindrical coordinate system at the tip as shown in Figure 4. The standard maximum principal stress criteria stipulate that fracture propagation occurs in the direction of maximum principle stress, which also corresponds to zero shear stress. The available fracture directions are limited to the existing finite element faces, so the face with the maximum hoop stress found using a relation for hoop stress

$$\sigma_\theta(r, \theta) = \frac{1}{(2r)^{0.5}} K(\theta) = \frac{1}{(2r)^{0.5}} \cos\frac{\theta}{2} \left[K_I \cos^2\frac{\theta}{2} - \frac{3}{2} K_{II} \sin\theta \right], \tag{25}$$

as given in [24]. The face with the highest hoop stress, namely, the greatest $K(\theta)$ value, is assigned the highest rupture priority when compared with the other faces attached to the edge. Because the topological update of the mesh typically affects multiple face elements, one face reaching the rupture criteria do not immediately trigger a topology update. The topology update logic is briefly described in the next section.

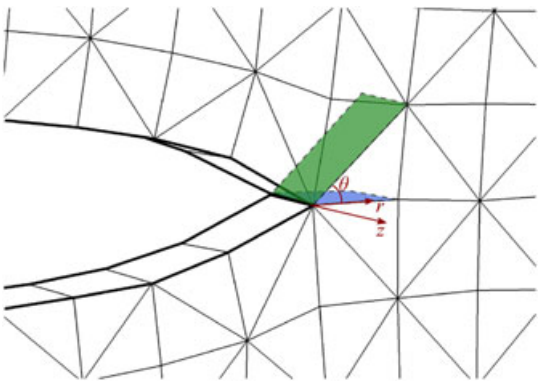

Figure 4. The mixed-mode rupture criterion determines along which face connected to the fracture front edge should the fracture propagate. [Colour figure can be viewed at wileyonlinelibrary.com]

DOI: 10.1002/nag

4.3. Node-centered logic for topological updates

The logic for the topology change uses a node-centric approach presented in [25, 26]. In the setting of a discrete finite element mesh, the creation of newly fractured surfaces requires a series of modifications to the mesh topology. These topology changes entail splitting (i.e., duplications) of nodes, edges, faces, as well as modifications to the elements that are connected on either side of the rupturing face. One challenge is that the splitting of a face can necessitate edge and node duplications that imply the splitting of a neighbor face. The simple case in Figure 5 illustrates such complexities. Consider an internal plane in a piece of solid structurally meshed with only nine elements on each horizontal cross-section. If the mechanical criterion has indicated that face #4 and only #4 is ready for fracturing, no topological change can accommodate this without affecting other faces. For instance, if we were to duplicate node a, it is required that faces #1, #2, and #5 undergo the splitting process as well. Therefore, we will have to hold face #4 intact and wait for other conditions to be met before we can duplicate a node. When the mechanical fracturing criterion later indicates that faces #1, #2, #4, and #5 can be split, we will need duplicate nodes a, b, c, and d altogether. In a different scenario, if the mechanical criterion suggests that face element #2 is ready for fracturing, it is then sufficient to accommodate this by duplicating *node c*.

The method employed to update the topology as demanded by the rupturing of faces is described in detail in [26] and [25]. Briefly, under this approach, after all the rupture-ready faces have been identified in each timestep following the method in the previous section, each node of the mesh is inspected to determine if the mesh should be split at that location. If a closed path can be found around a node traversing the rupture-ready and external faces attached to that node, then the node is marked for splitting. Once all nodes have been inspected, new nodes are generated from the split set along with any common edges, and faces, and the mesh topology is updated accordingly.

4.4. Topology change in parallel

When working in distributed memory parallel computing environments, the discretized problem is typically split into domains, with each processor assigned to a given domain. On each domain, there usually exists 'local' objects, and 'ghost' objects. The local objects are owned by the current domain, and the ghost objects are owned on neighboring domains but are represented on the current domain to facilitate calculation of quantities required by the numerical method. Thus, certain topological

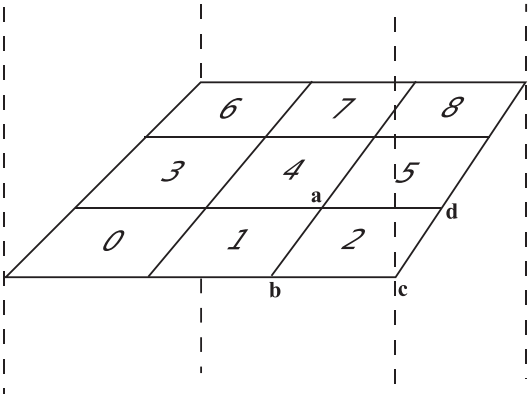

Figure 5. A simple example illustrating the topological consequences of slipping a face element.

DOI: 10.1002/nag

objects such as nodes, edges, faces, and elements will be represented on multiple domains. The inter-object relations are assumed to be valid and consistent in all locations, and the synchronization of the data associated with these objects is typically a feature of the host simulation code.

Without careful attention, the mesh splitting scheme outlined in Section 4.3 may result in inconsistent mesh topologies when applied to boundary objects in adjacent parallel partitions. Consider a mesh that is partitioned for distributed memory parallelism, where simultaneous duplication of spatially adjacent nodes occurs on neighboring domains. Figure 6 illustrates two scenarios where this situation occurs between two neighboring domains. In both scenarios, the local objects (i.e., objects owned by a given domain) are shown in back, while the ghost objects (objects owned by a neighboring domain) are shown in red.

Figure 6(a) illustrates the scenario in a two-dimensional problem. If Domain 0 duplicates node 0, then duplication of face 0 is required. The duplication of face 0 requires that connected edges are duplicated, and connectivities are modified to reflect the new node/edge/face. If domain 1 duplicates node 1, then face 0 must also be duplicated, and similarly, connectivities are modified to reflect the new node/edge/face. If Domains 0 and 1 are free to duplicate objects independently of each other, then the same object can be duplicated at the same time on both domains. As such, there will exist two copies of the duplicated faces and edges, which would require an algorithm to synchronize the ownership, inter-object connectivities, and field data of the new objects across domains.

Figure 6(b) illustrates a three-dimensional mesh with the two neighboring domains rotated away from each other such that the domain boundary is visible on both sides of the boundary. If the fracture is propagating in the direction in the plane of the domain boundary, then spatially adjacent nodes are commonly duplicated at the same time. Again, Domain 0 will duplicate 'node 0' and Domain 1 will duplicate 'node 1', which results in each partition duplicating the highlighted 'face 0' and associated edges. If the domains are allowed to change topology independently of each other, then one must develop a robust algorithm to enforce consistency after the duplications have occurred. Such a task may be feasible in two-dimensional problems, but the complexity becomes significantly greater in a three-dimensional setting.

Rather than allowing partitions to change topology independent of each other, the proposed method utilizes an independent domain mapping scheme to allow consistent topology change in a distributed memory parallel computing environment. In this scheme, each domain is assigned tag such that all neighboring domains have a different tag. Nodes within each domain are labeled as 'internal' or 'external' to signify their interdependence with neighboring domains such that internal nodes have no dependence on ghost objects and do not affect ghost objects on neighboring domains, while external nodes have a dependence/influence on neighboring domains. To ensure consistent changes in mesh topology, the external nodes on all domains with a given tag are processed concurrently, and the resulting topological changes are sent to the neighboring domains. This results in a situation where each domain is able to generate topology changes freely but is required to send/receive topology changes to/from neighboring domains. Figure 7 shows a typical tagging

Algorithm 1 Algorithm for mesh splitting in parallel

Require: Set Rupture Criteria for Faces
Require: Domains/partitions given *nTags* tags
1: **for** tag in *nTags* **do**
2: **if** tag == *domainTag* **then**
3: Process "external nodes" for separation
4: **else**
5: Process $\frac{1}{nTags}$ of the "internal nodes" for separation
6: **end if**
7: tag communicates any topological changes for both objects owned by tag and objects that are ghosts on tag to neighbor partitions.
8: Communicate any topological changes that have occurred on objects owned by the neighbor partition to its neighbor partitions.
9: **end for**

DOI: 10.1002/nag

scheme on a two-dimensional cartesian partitioning scheme. In this realization of the scheme, all external nodes on partitions with tag A are processed, and then, topology changes are communicated to neighboring domains (B, C, D). This is then repeated for partitions with tag B, then C, then D. If a three-dimensional cartesian partitioning scheme is used, then there are eight independent tags that are required for this procedure, although in the general case of non-cartesian partitioning there is not a fixed number of tags. The idling of processors associated with partitions that are waiting to process may be avoided by intelligently processing a portion of the internal nodes on domains not currently engaged in processing of external nodes. This results in a robust and scalable algorithm, which is outlined in Algorithm 1.

4.5. Initialization of newly fractured fluid volumes

In a fully discrete treatment, such as the approach taken by the proposed method, the fracture is always assumed cut and entire face/element. In this approach, fracture extension results in an instantaneous increase in crack area, and potentially an instantaneous increase in total fluid volume. The manner in which new fluid volumes are initialized is a crucial factor in the 'smoothness' of the fracture process, and several methods have been attempted to provide a smooth introduction of new fracture area/fluid volume. However, the added complexity/non-linearity of methods that attempt to provide true 'smoothness' has shown limited value when evaluating the overall performance of the proposed method. Therefore, a simple approach is applied where newly generated surfaces are given a very small initial volume (so that the volume may never be zero) and are initialized with a neutral pressure (i.e., zero), The development of a technique that smoothly introduces new fracture area/fluid volume is an important topic that should be investigated further in future studies.

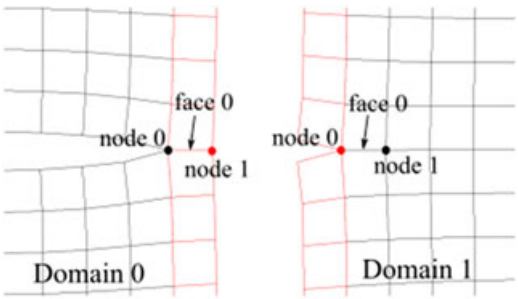

(a) 2-Dimensional example of generation of inconsistent topology.

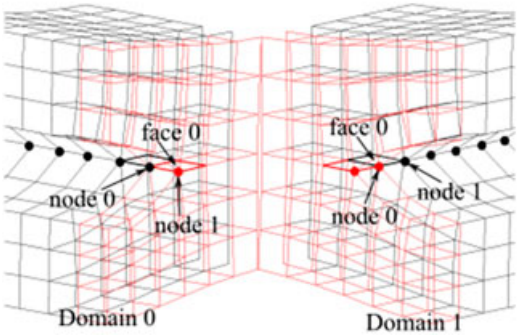

(b) 3-Dimensional example of generation of inconsistent topology.

Figure 6. Example scenario that results in the generation of inconsistent topology. Domain local objects are displayed in black, while ghost objects are displayed in red. If topology change is allowed independently, Domain 0 may split 'node 0', and Domain 1 may split 'node 1' with both domains attempting to duplicate 'face 0'. [Colour figure can be viewed at wileyonlinelibrary.com]

DOI: 10.1002/nag

5. NUMERICAL EXAMPLES

In this section, we compare simulations that utilize the proposed method against analytical solutions, results from lab scale experiments, and finally conclude by applying the method in a field scale study.

The analytical examples consist of three well-accepted solutions for a hydraulically driven fracture problems. In the first verification case, the two-dimensional plane strain hydraulically driven fracture described by Khristianovic *et al.* [27] and Geertsma *et al.* [28] (typically referred to the KGD problem) is compared with the solutions provided by Detourney [29]. In the second verification case, a three-dimensional radial hydraulically driven fracture (i.e., a penny shaped crack) is compared with the solutions of Savitsky and Detourney [30]. In the third verification case, a fixed height lateral fracture (PKN after Perkins, Kern [31] and Nordgren [32]) is compared with the solutions of Nordgren [32].

In addition, the proposed method is validated against results from a hydraulic fracture experiment given by Rubin [33]. Finally, the results from a field-scale three-dimensional simulations are presented to demonstrate the effectiveness of this approach in modeling real-world engineering problems.

The simulations presented in this study were run on Lawrence Livermore National Laboratory's Cab supercomputing cluster. The Cab cluster consists of 2400 Intel Xeon E5-2670 processors (19,200 cores) for batch processing. The GEOS code framework [13, 14] is utilized to simulate all numerical examples presented.

5.1. Verification problems

5.1.1. Plane strain fracture (KGD). The hydraulically driven plane strain fracture problem, or KGD problem, describes a single hydraulic fracture is a infinite half-space (Figure 8(a)). To maintain consistency between the numerical simulations and the assumptions in [29], we specify linear elastic response of the solid material, incompressible fluid response, and that the fluid is able to achieve unbounded negative pressures without cavitation. To assure that there are negligible boundary effects, the problem domain extends 1 km from the source. The problem contains 43,200 hexahedral elements and is run to a simulation time of 100 s. The simulations approximately 3.05 s per timestep utilizing 16 cores (single computing node) in a distributed memory configuration. The relevant problem parameters are outlined in the first column of Table I. Simulations were performed with fixed timesteps ranging from 0.25 to 8.0 s to assess the influence of timestep on accuracy. Figure 8(b) shows the deformed mesh from a GEOS simulation using the proposed method after 100 s of simulation time. The color of the solid elements represents the material stress normal to the

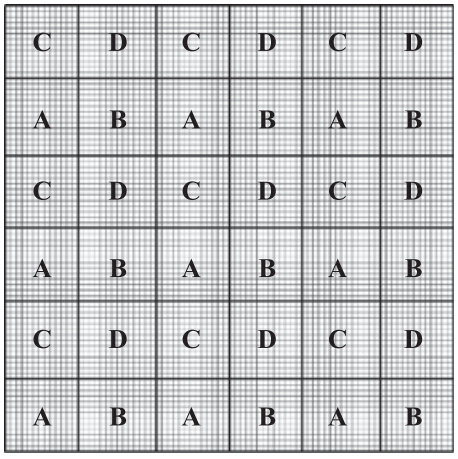

Figure 7. Illustration of partition tagging scheme in two-dimensions. Each letter represents a tag that signifies the order in which topology changes may be made on the boundary objects of a partition.

DOI: 10.1002/nag

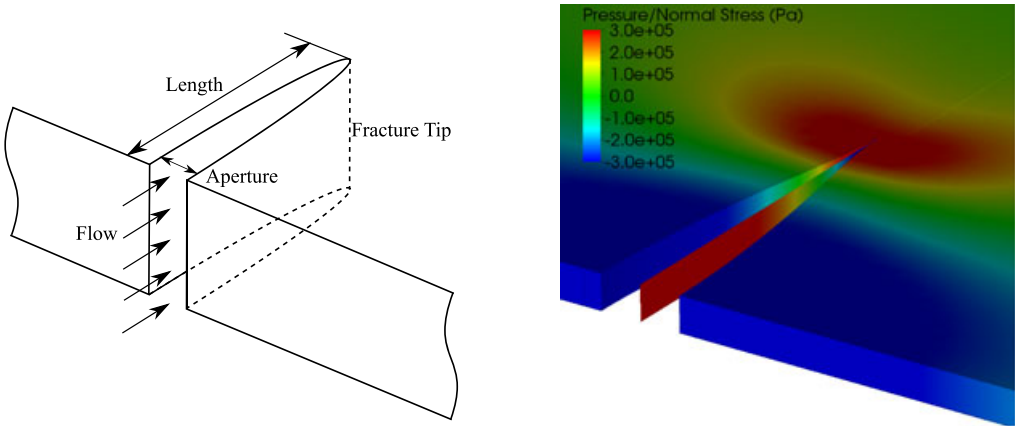

(a) Geometry of KGD problem.

(b) Image of KGD problem from GEOS simulation. Fluid pressure in fracture is shown on FVM mesh, while solid stress normal to crack propagation direction on FEM mesh. Body deformations are on image are magnified x10,000

Figure 8. Description and results for a plane strain fracture problem (KGD geometry). [Colour figure can be viewed at wileyonlinelibrary.com]

Table I. Material properties and model parameters for verification simulations.

Simulation	KGD	Radial	PKN
Solid Young's modulus, E (GPa)	30	30	30
Solid Poisson's ratio, ν	0.25	0.25	0.25
Solid toughness (baseline), K_{Ic} (MPa $/m^{0.5}$)	0.1	3.0	0.1
Fluid dynamic viscosity, μ (Pa s)	0.001	0.001	0.001
Injection rate, q (m^3/s)	0.002[a]	0.053	0.04
Carter's leak-off coefficient[b], C_L ($mm/\sqrt{s}$)	NA	0.15	0.15
Fracture height, h (m)	NA	NA	20

[a] per m thickness
[b] For leak-off-dominated cases only; zero otherwise.

plane of the fracture (compression is negative), and the color of the fracture mid-plane illustrates the fluid pressure in the crack (compression is positive). The effects of the fluid pressure on the deformation and stress field in the solid are easily observed, as the fluid pressure and the material stress normal to the fracture plane are virtually identical.

The GEOS simulations are plotted against the asymptotic solutions for the 'zero toughness' assumption in Figure 9. The results for the temporal evolution of fracture length, injection pressure, and fracture aperture near the injection point are plotted through the end of the simulation ($t = 100$ s) in Figure 9(a). In addition, to the evolution plots, Figure 9(b) shows the values of aperture and fluid pressure along the length of the fracture at the end of the simulation ($t = 100$s). The simulation results show that the error decreases with reductions in timestep and are in excellent agreement with the asymptotic solutions below $\Delta t = 1.0$ s. The disparity between the converged solution and the numerical solution appears to increase with $O(\Delta t)$ for timesteps above 1.0 s. While this is expected, we note that the discrete rate of fracture occurs at a rate slightly less than 1 finite element face/finite volume element per second. Thus, using a timestep significantly greater than 1 s is undesirable because it requires the calculation of flow between newly formed finite volumes, both of which are seeded with identical states at the beginning of the timestep. Therefore, we impose a heuristic limitation on the timestep such that fractures do not advance more than one spatial discretization in the direction of the fracture propagation during a single timestep.

DOI: 10.1002/nag

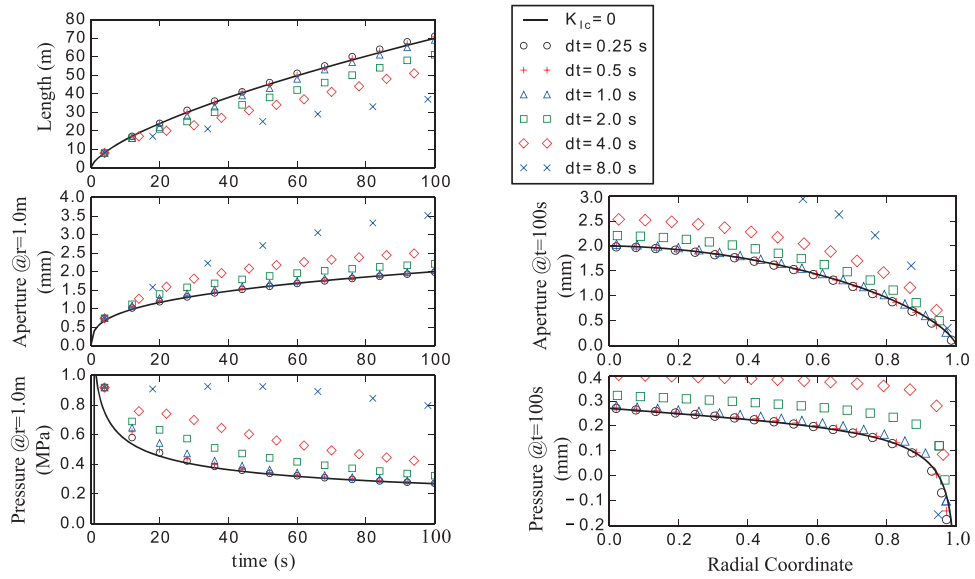

(a) Plot of fracture half-length, near-wellbore aperture, and near-wellbore pressure plotted versus time. In this case, the term "near-wellbore" means a distance of 1m from the injection point.

(b) Plots of aperture and fluid pressure versus radial coordinate at end of simulation.

Figure 9. Simulation results for a plane strain fracture (KGD geometry) for varying timesteps plotted agains zero-toughness asymptotic solution given by [29]. [Colour figure can be viewed at wileyonlinelibrary.com]

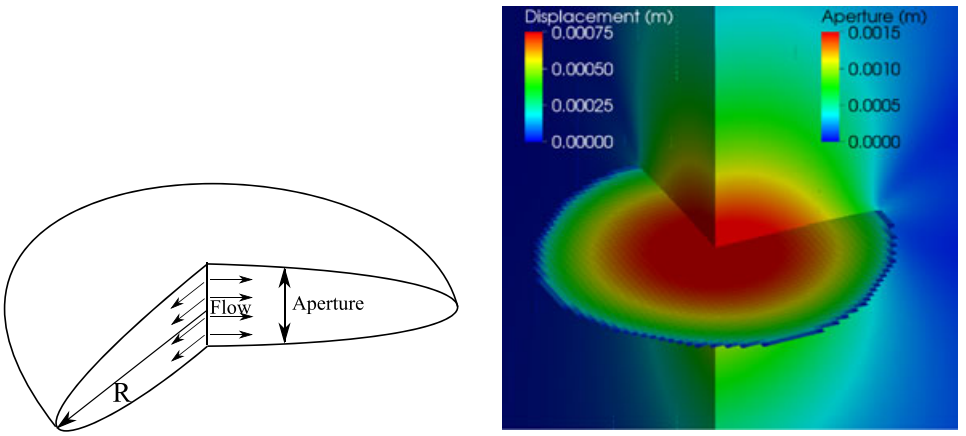

(a) Geometry of radial fracture problem.

(b) Image of radial fracture problem from GEOS simulation. Fracture aperature is shown on FVM mesh, while displacement magnitudes are shown on FEM mesh. Body deformation are magnified x10,000

Figure 10. Geometry and simulation results for a radial fracture. [Colour figure can be viewed at wileyonlinelibrary.com]

5.1.2. Radial fracture problem. The simplest three-dimensional problem consists of a single radial fracture propagating from a point source at the center of the radial geometry (Figure 10(a)). As with the previous verification problem, we restrict our numerical solutions to the assumptions used in [30]. Namely, we specify linear elastic response of the solid material, incompressible fluid response, and that the fluid is able to achieve unbounded negative pressures without cavitation. To model this

DOI: 10.1002/nag

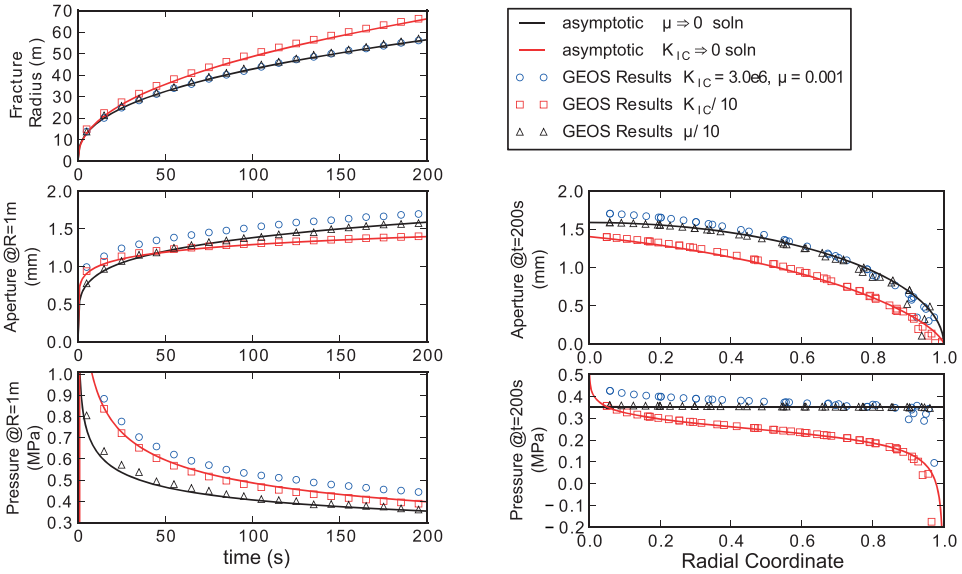

(a) Plot of fracture radius, near-wellbore Aperture, and near-wellbore pressure plotted versus time.

(b) Plots of aperture and fluid pressure versus radial coordinate at end of simulation.

Figure 11. Simulation results for a radial fracture plotted against zero-toughness and zero-viscosity asymptotic solution given by [30]. GEOS simulations are also shown for reductions in toughness as well as reduction in viscosity for comparison with asymptotic solutions. [Colour figure can be viewed at wileyonlinelibrary.com]

problem, a 1-km cube is discretized with 2-m element sizes in the region surrounding the injection point and progressively larger elements in the far field using the two symmetry planes to reduce the problem to quarter scale, for a total of 2,487,680 elements. The simulation is conducted across 320 cores (20 nodes) and requires approximately 19 s per timestep. Material properties and pumping rates are specified in Table I.

The results of three GEOS simulations, zero toughness (i.e., viscosity dominated), and zero viscosity (i.e., toughness dominated) asymptotic solutions of [30] are plotted in Figure 11. Note that for the direct numerical simulation such as the one presented here, assumptions such as zero toughness and zero viscosity are unnecessary, as these cases, as well as all intermediate cases and transitions between toughness-dominated and viscosity-dominated regimes are handled naturally by the proposed method. The first GEOS simulation denoted in the legend of Figure 11 corresponds to the parameters in Table I. These parameters represent an intermediate case between the valid ranges of the viscosity dominated and toughness dominated assumptions. The following two GEOS simulation in Figure 11 have parameters identical to Table I except for reductions in viscosity in one case and reductions in toughness for the other. These simulations are used for purposes of comparison with the corresponding asymptotic solutions. The fracture radius is calculated by taking the total area of the fracture, and inferring a radius assuming a perfect circular shape ($Radius = \sqrt{Area/\pi}$). There is a small shape error owning to mesh dependency, with fracture radius in the diagonal direction slightly lagging the cartesian directions, however the variation in the radius typically less than 5%. Also, note that because of the discrete nature of the simulations, the wellbore aperture and pressure values are not at the theoretical singular point source but rather located in the center of the finite volumes closest to the point source. The temporal evolution of fracture radius, near-wellbore aperture, and near-wellbore pressure for both the numerical results and the asymptotic solutions are shown in Figure 11(a).

The results from the reduced viscosity GEOS simulation ($\mu/10$) are nearly identical to the toughness dominated ($\mu \rightarrow 0$) asymptotic solution, and the results from the reduced toughness GEOS simulation ($K_{IC}/10$) are nearly identical to the viscosity dominated ($K_{IC} \rightarrow 0$) asymptotic solution. Similarly, the plots of near-wellbore fracture aperture and near-wellbore fracture pressure

DOI: 10.1002/nag

versus time correlate very well with the asymptotic solutions. The aperture and fluid pressure profiles at the end of the simulation ($t = 200s$) are illustrated in Figure 11(b). The quantities are plotted against the radial coordinate – defined by the distance between the center of a fluid element and the injection point normalized by the total fracture radius. As is the case with the temporal plots, the profiles correlate very well with the solutions for both the viscosity dominated and toughness dominated cases.

The intermediate case corresponding to the values in Table I does not fall within the applicable ranges of either the viscosity-dominated or toughness-dominated assumptions, and as expected, the numerical solution does not correlate well with either of the asymptotic solutions. An explanation for this behavior has to due with the fact that the intermediate case has significant energy dissipation from both fluid viscosity and fracture energy. An examination of the time history plots in Figure 11(a) shows that the intermediate case displays slightly lower values of fracture radius, and significantly higher values of injection aperture and pressure when compared with the asymptotic solutions.

A similar examination of the plot of the distribution of fluid pressure in Figure 11(b) clearly shows that with the results from the intermediate case exhibit a higher injection pressure than the toughness-dominated case, a tip pressure below the toughness-dominated case but above the viscosity dominated case, and a pressure that is generally higher than both cases across the fracture. The plot of aperture distribution in Figure 11(b) follows the expected trend of a slightly higher value for the majority of the fracture (corresponding to a higher fluid pressure), despite having slightly lower values than the toughness-dominated case in the near tip region.

A brief discussion of the effects of adding a second dissipation mechanism to each of the asymptotic solutions is useful to understand the combined dissipation mechanisms present in the intermediate case. Starting from the assumptions of the viscosity-dominated solutions, the effects of adding fracture toughness must result in a higher fluid pressure at the fracture tip in order to overcome the additional (relative to zero) toughness. This will result in a shallower pressure drop from the fracture tail to fracture tip, as there must be a greater accumulation of fluid at the tip as per the preceding statement. There will be a higher overall pressure distribution throughout the fracture, and this will result in larger aperture values across the fracture. Because the fluid is incompressible, and thus the volume of injected fluid is for every point in time for each of the cases, the fracture radius must be lower to accommodate the higher aperture distribution.

One advantage of using a numerical solution scheme to solve the governing equations is that the governing equations dictate the simulation results. If the governing equations are applicable for the desired parameter space, and the numerical implementation does not make any assumptions that reduce the range of applicability, then you are guaranteed a solution that adheres to the physics dictated by the governing equations. This example shows that the proposed method is able to simulate of any combination of viscosity and fracture toughness, and that the solution does not require any limiting assumptions that would limit its applicability.

5.1.3. Verification with lateral hydraulic fracture. While useful for verification, the radial fracture geometry presented earlier has somewhat limited applicability to field scale simulations. Typically, the assumed geometry of field scale hydraulic fractures consists of a hydraulic fracture vertically bounded (either by toughness or in-situ stress contrasts in neighboring material) in a layer and that propagates many times the thickness of that layer (Figure 12(a)). These geometric assumptions are classically addressed by the PKN solution [31, 32]. The proposed method has been applied to a lateral fracture propagation simulation specifying a 20-m thick target layer with upper and lower toughness bounds with a fracture the initiates within the target layer and is centered within a 2-km (cubic) domain. The model consists of 1,052,480 hexahedral elements and was run on 256 cores (16 nodes), with runtimes of 10 s per cycle. As in the solution given by [31, 32], the fluid pressures are not allowed to attain negative values. The material properties used in the simulations are given in Table I.

Figure 13 plots a comparison of results from the numerical simulation and the PKN solutions of Nordgren [32]. The plots of wellbore aperture and fracture length are in excellent agreement with the Nordgren solution, even at early time when the fracture length is of the same order as

DOI: 10.1002/nag

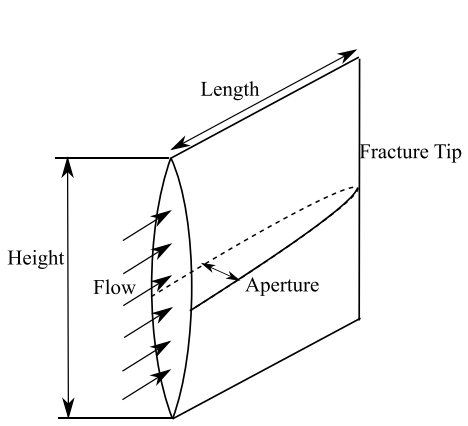

(a) Geometry of PKN problem.

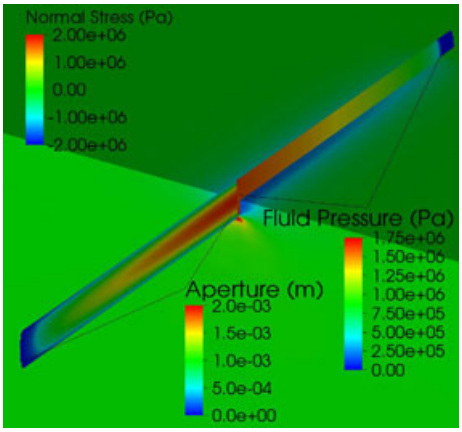

(b) GEOS simulation result of the PKN problem. Fracture color scales indicate pressure and aperture, while the color scale for the continuum indicates stress in the direction normal to the fracture.

Figure 12. Description and GEOS simulation image for PKN problem. [Colour figure can be viewed at wileyonlinelibrary.com]

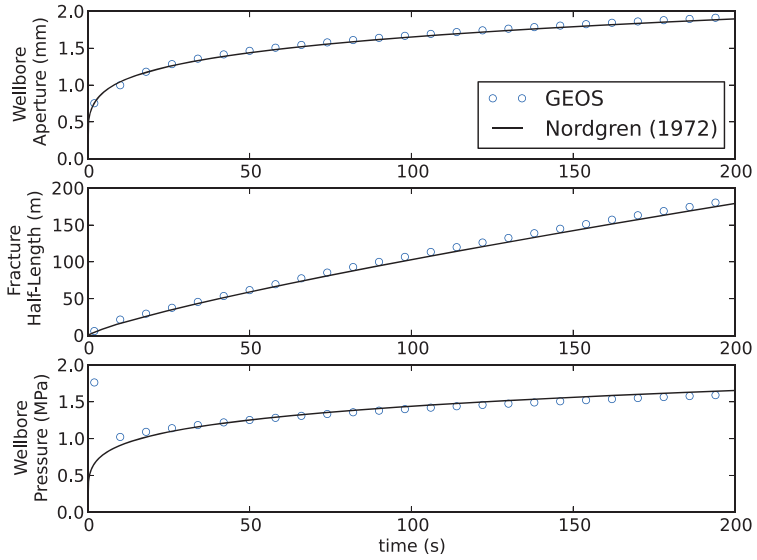

Figure 13. Comparison of GEOS against the Nordgren solution [32] for the PKN problem.[Colour figure can be viewed at wileyonlinelibrary.com]

fracture aperture. The plot of pressure at the source shows significant deviation from Nordgren's solution at early time, before the conditions of the problem match the geometric assumptions of the Nordgren solution (i.e. the fracture length is much greater than the height and flow is in the direction of fracture propagation), and the solution asymptotes towards Nordgren's solution as the fracture length increases (l/H exceeds $\sim$5).

5.1.4. Verification with leak-off-dominated fracture propagation. The three sets of verification cases earlier all assumed zero leak-off into the rock matrix surrounding the fracture. In this section, we perform an additional radial hydraulic fracturing simulation and a lateral hydraulic fracturing (PKN) simulation using identical parameters as the previously presented examples, except for application of a Carter's leak-off model with a coefficient of 0.15 mm/$\sqrt{s}$. The analytical solutions of the high leak-off approximation for the lateral hydraulic fracture half-length and radial fracture radius

DOI: 10.1002/nag

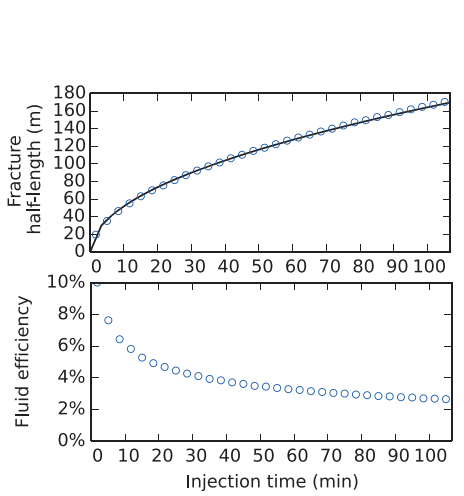

(a) Lateral Fracture: Plot of fracture half-length and fluid efficiency plotted versus time.

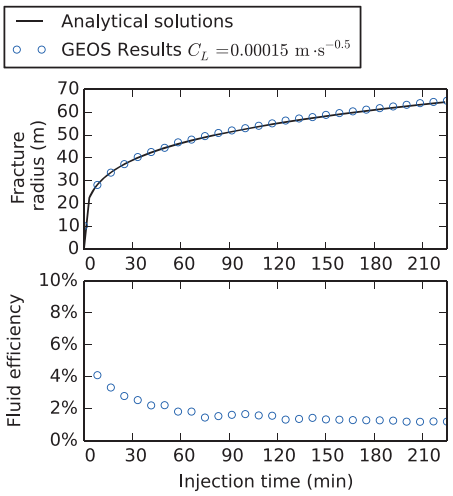

(b) Radial Fracture: Plot of fracture radius and fluid efficiency plotted versus time.

Figure 14. Simulation results for lateral hydraulic fracture and a radial hydraulic fracture, both with a high Carter's leak-off coefficient. Analytical solutions for leak-off dominated are plotted for comparison. Both cases use the same parameters shown in Table I except that the radial fracture uses a solid toughness of $0.1\mathrm{MPa}/\sqrt{\mathrm{m}}$. [Colour figure can be viewed at wileyonlinelibrary.com]

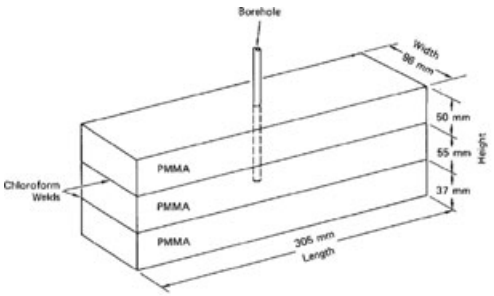

(a) Diagram of Experiment taken from Rubin [33].

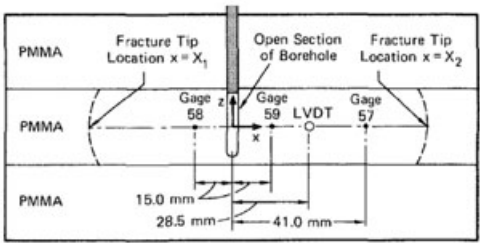

(b) Diagram indicated instrumentation locations.

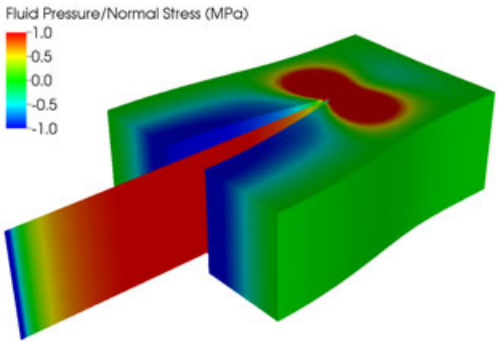

(c) Image of fracturable layer from GEOS simulation (displacement magnified x5000)

Figure 15. Experimental configuration from [33] (a) and equivalent GEOS simulation (b). [Colour figure can be viewed at wileyonlinelibrary.com]

are available in Mack and Warpinski [34] and not repeated here. The comparison between the analytical solutions and GEOS simulation results for the lateral fracture is shown in Figure 14(a), and the results for the radial fracture are shown in Figure 14(b). The values of fracture extent match the analytical solutions very closely for both radial fracture and lateral fracture. The fluid efficiency,

DOI: 10.1002/nag

which is the percentage of the total injected fluid that remains in the fracture, is also shown for both cases. The very low efficiencies at later injection times, less than 4% for the lateral fracture and less than 2% for the radial fracture, confirm that these two simulated hydraulic fractures are in the leak-off dominated regime.

5.2. *Validation with experiment*

A validation test was performed simulating a lateral hydraulically fracture experiment in PMMA presented in [33]. The experimental setup, shown in Figure 15(a), consists of three weakly bonded layers of PMMA, with the fracture confined to the middle layer. Unlike the archetypal PKN problem, the experiment has boundaries that are relatively close to the fracture that serves to influence the behavior of the hydraulic fracture. The material properties for PMMA and the fracturing fluid cited in [33] are used in the GEOS simulation and summarized in Table II. The discussion in [33] indicates that the bond between layers is such that there is very little resistance to slip, and that the experiment behaves similar to that of a plane strain problem. As such, the bond/fracture toughness between the layers is specified to be near zero, and thus, the upper and lower layers of PMMA serve only to restrict the flow of fracturing fluid away from the main fracture. This results in a problem very similar to the KGD geometry, except for the presence of traction free external boundaries in relatively close proximity to the fracture. The instrumentation layout for this experiment consisted of one pressure gage for the wellbore pressure, three pressure gages along the length of the fracture (−15, 15, and 41 mm), one LVDT measuring the fracture opening 28.5 mm from the wellbore, and visual images to measure the extent of fracture taken at regular intervals (Figure 15(b)).

Table II. Material properties and model parameters for PMMA given in [33].

Young's modulus, E (GPa)	3.28
Poisson's Ratio	0.367
Rock toughness, K_{Ic} (MPa $/m^{0.5}$)	1.2
Viscosity, μ (Pa s)	97.7
Injection rate, q (m^3/s)	73.2(10^{-9})

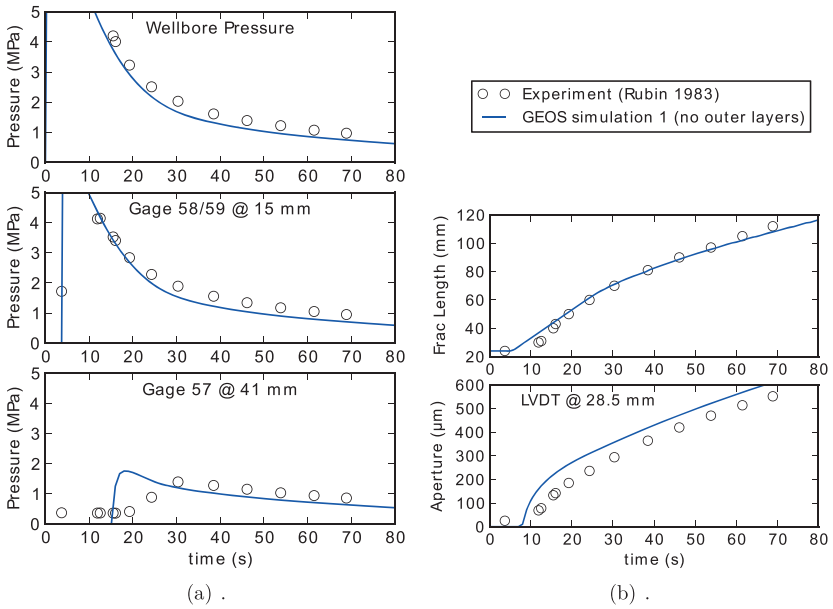

Figure 16. Comparison of GEOS simulation output versus experimental results from Rubin [33]. [Colour figure can be viewed at wileyonlinelibrary.com]

DOI: 10.1002/nag

An illustration of the GEOS simulation is shown in Figure 15(c), where the full fracture plane is shown, while half of the specimen is cut away for easier visualization. The material stresses (σ_n) are equal to the fluid pressure on the fracture surface and drop to zero at of the outer boundary of the PMMA block as expected. Time history plots of the experimental data and simulation results for the three pressure gage locations, the fracture length, and the fracture aperture LVDT are shown in Figure 16. The simulated fracture length and aperture as a function of time correlates well with the experimental data (Figure 16(b)). There appears to be some early fracture growth in early time (5–15 s), while a slight under-prediction of fracture length appears at later time (50 s). The fracture aperture appears to have a moderate error (25% peak error) when compared with experiment values, although the magnitude of the error does not increase with increasing aperture.

The simulated wellbore pressure slightly under-predict experimental fluid pressures, which is expected as the simulation results show the pressure at the center of the finite volume closest to the wellbore rather than the wellbore pressure itself. The pressures at the locations of gage 58/59 ($\pm$15 mm) also show a slight under-prediction of the simulations when compared with experimental data, and the plot of pressure at gage 57 shows that the simulation achieves an earlier arrival time than the experiment, which correlates with the early time overshoot of the fracture length. The general agreement between the numerical simulations and the experimental data provides an adequate verification of the method.

5.3. *Field scale simulation*

This section demonstrates GEOS's ability to simulate a reservoir stimulation job at the field scale under conditions of a varying *it situ* stress field, as well as a large number of natural fractures. In this example, fluid is injected into single hydraulic fracture that interacts with a natural fracture network. Cases where fluid is injected into multiple fractures to model a multi-cluster stage has been demonstrated in previous work [35].

The *in situ* stress profile in the rock formation near the injection depth is shown in Figure 17(a). Three layers can be identified based on the minimum horizontal stress (S_{hmin}) profile. The injection takes place ($z = 0$), which is at the mid-height of the constant S_{hmin} Layer 2 (z from -25 to 25 m). There is a 'stress barrier' of 0.3 MPa at the interface between Layer 1 (z from 25 to 75 m) and Layer 2, which results in an increase in the required pressure for the hydraulic fracture to propagate into Layer 1 from Layer 2. However, once the fracture breaks into Layer 1, the presence of a relatively high vertical gradient of S_{hmin} (12.5 kPa/m compared with the hydrostatic pressure gradient of 9.8 kPa/m) will drive the fracture to propagate upwards until it is arrested by the 2-MPa stress barrier

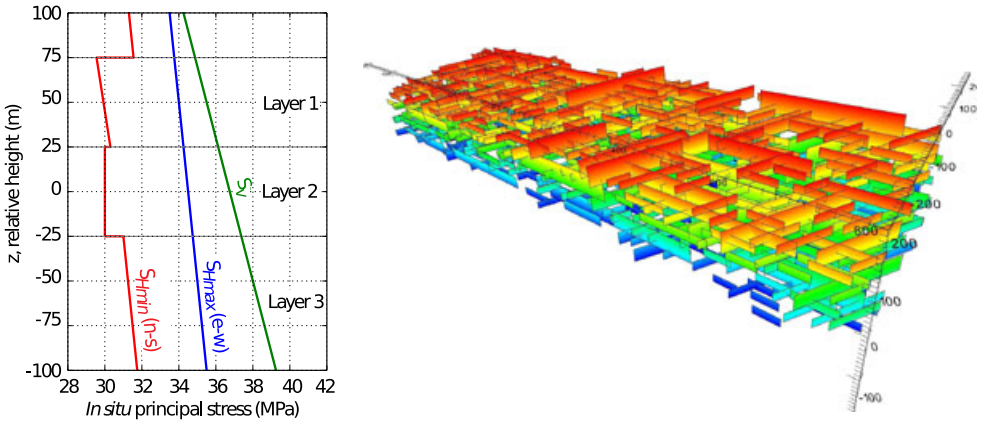

(a) The *in situ* stress profile

(b) The random discrete fracture network (DNF). The DFN is colored based on vertical coordinates.

Figure 17. The description of the *in situ* stress profile, and discrete fracture network for the field scale simulation. The coordinate system for this system is defined with the origin at the injection point, the x-axis pointing east, the y-axis pointing north, and the z-axis pointing up. [Colour figure can be viewed at wileyonlinelibrary.com]

DOI: 10.1002/nag

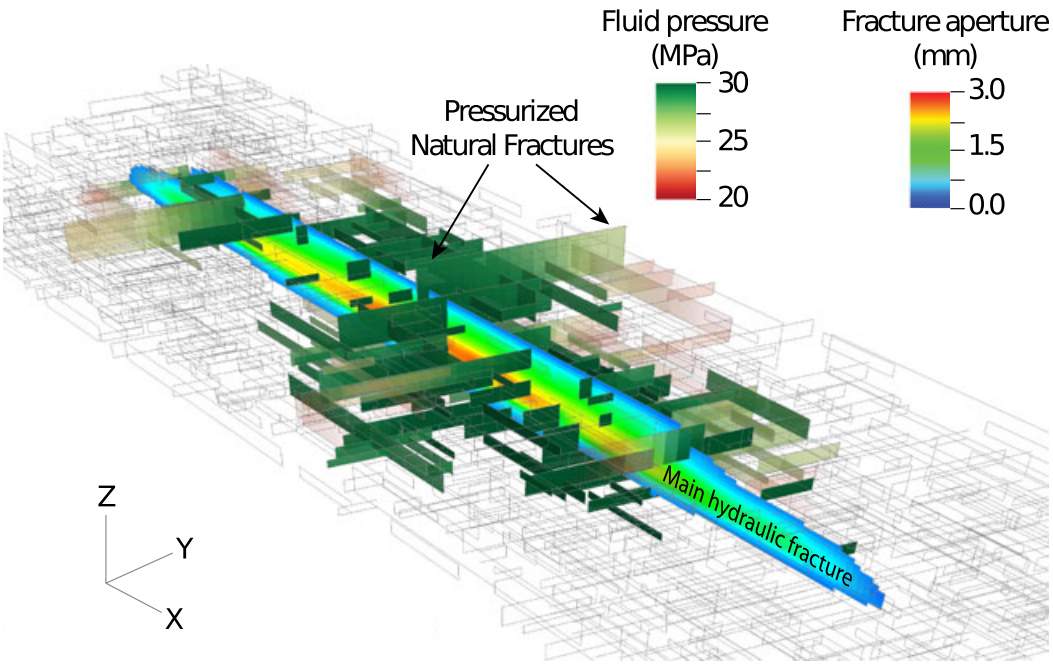

Figure 18. Overview of the hydraulic fracturing simulation with the main hydraulic fracture colored based on aperture and pressurized natural fractures colored based on fluid pressure. Natural fractures that have not been pressurized by fluid from the hydraulic fracture are rendered transparent with only the perimeters shown as gray lines. The main hydraulic fracture in the figure is colored based on the fracture aperture distribution. [Colour figure can be viewed at wileyonlinelibrary.com]

at the top of Layer 1. The stress barrier between Layers 2 and 3 is 1.0 MPa, discouraging but not necessarily preventing the fracture from propagating downwards into Layer 3. The vertical gradient of S_{hmin} in Layer 3 is 10.0 kPa/m, only slightly greater than the hydrostatic pressure gradient.

The *in situ* pore pressure is 20 MPa at the injection depth and follows a standard hydrostatic gradient. In this example, the permeability of the rock matrix is ignored, and therefore, the pore pressure is only used to initialize the fluid pressure within *in situ* fractures. All rock layers have the same elastic properties: a Young's modulus of 30 MPa and a Poisson's ratio of 0.25. The injection fluid has a dynamic viscosity of 0.001 Pa· s, and the injection rate remains constant at 0.053 m^3/s (20 barrels per minute).

The reservoir is characterized by a discrete fracture network (DFN) consisting of two vertical fracture sets (Figure 17(b)). The strikes of the two sets are 30° (Set A) and 90° (Set B) east of north. The fracture lengths in both sets follow a power-law distribution with a lower limit of 50 m, an upper limit of 400 m, and an exponent of 2.0. The aspect ratios follow a uniform distribution between 0.1 and 0.25. Within the core problem domain of (±800m, ±250m, and ±100m), 940 fractures are randomly generated, following the aforementioned distributions with a total area of 3,000,000 m^2, which is corresponding to a fracture density of 0.019 m^{-1}. Natural fractures and the main fractures that are attached to an source (i.e., intersect the wellbore) are treated in an equivalent manner in the proposed method; thus, natural fractures may extend if that is what is dictated by the problem physics. In other words, natural fractures are indistinguishable from the any other fracture, except for the fact that, in the case of a natural fracture, the alteration of mesh topology required to define a fracture occurs during the initialization stage.

The simulation domain has a core region covering the DFN dimensions with relatively high mesh resolution of 8.0, 13.86, and 6.25 m in the x-directions, y-directions, and z-directions. Surrounding the core region is a coarsely resolved region extending the domain to ± 1400m, ± 500m, and ± 250m in the three directions, respectively.

The entire mesh consists of approximately one million prism elements. As GEOS allows fracture generation and fracture propagation along inter-element faces, the mesh is structured to incorporate grid-lines and faces parallel to the Sets A and B directions.

DOI: 10.1002/nag

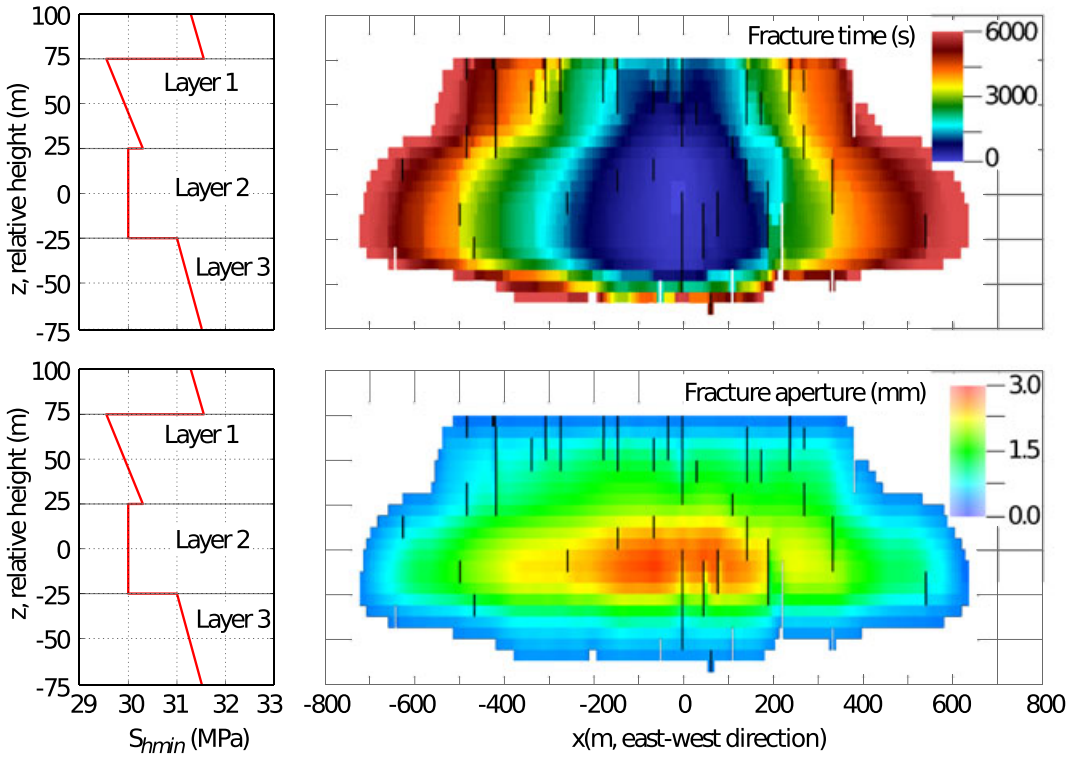

Figure 19. The projection of the main hydraulic fracture at 6300 s onto the x–z plane, colored based on aperture using the same color map as that in Figure 18. The *in situ* minimum principal stress profile is also shown with aligned z-coordinates for reference. The black vertical lines on the fracture plane denote the intersections between natural fractures and this hydraulic fracture. Note that the image is shrunk in the x-direction by four times for better visualization. [Colour figure can be viewed at wileyonlinelibrary.com]

The responses of the hydraulic fracture and the DFN to 105 min of stimulation are illustrated in Figure 18. The opacity the natural fractures is determined based on the fluid pressure inside: fractures with pressure at or below the *in situ* pore pressure are completely transparent, and the perimeters of these fractures are shown as gray lines. The fluid pressure in natural fractures that have been connected to and stimulated by the fluid from the hydraulic fracture is denoted by opacity and color. At 105 min into the stimulation, approximately 57% of the injected fluid remains in the hydraulic fracture, and 43% has leaked into the DFN.

To better observe features of the main hydraulic fracture, the fracture is projected onto the x–z plane in (Figure 19). The upper and lower parts of the figure show the fracture time (the time when each face element was split to extend the fracture) and fracture aperture, respectively. The intersections between the main hydraulic fracture and natural fractures are visualized as black vertical lines.

The overall shape of the fracture (and the shape at any given time as inferred from the fracture time plot) is consistent with the expected fracture behavior for the given stress profile. Within Layer 2, the fracture propagates farther at greater depths as a result of the uniform S_{hmin} value and the pressure gradient due to gravity. At horizontal locations where the fracture breaks into Layer 1, it propagates vertically all the way to the top of this layer until the propagation is hindered by the 2-MPa stress barrier. This strong upward propagation tendency in Layer 1 is driven by the greater-than-hydrostatic S_{hmin} gradient. Because of the small stress barrier between Layers 1 and 2, the fracture's lateral propagation in Layer 1 lags that in Layer 2. The fracture does break into Layer 3, but only near the center where pressure is relatively high. However, the downwards propagation in Layer 3 is greatly impeded by the S_{hmin} gradient.

The aperture field appears to be discontinuous across the intersections with natural fractures. Because there is a 'bypassing' mechanism that exists in the three-dimensional space, natural frac-

DOI: 10.1002/nag

tures of limited heights are unlikely to arrest hydraulic fractures even when the condition is unfavorable for direct crossing [36]. The shearing of the natural fractures, which are oriented 60° from the *in situ* principal stress directions, creates choke points at the intersections and thereby reduces the aperture of the hydraulic fracture near the intersection. Because of the choking effects of the natural fractures that intersect the hydraulic fracture in the range ($0m < x < 250m$), the fracture propagates towards the east more slowly than it does westwards. A further consequence of such shearing-induced choking is that it may affect the lateral placement of proppants.

This simulation involving a kilometer-scale reservoir, nearly 1000 natural fractures, and 2 h of simulation time, requires 288 intel Xeon E5-2670 cores running for 14 wall-time hours on a high performance computer (4032 CPU hours in total). Although more detailed analysis of the results is beyond the scope of the current work, this simulation demonstrates GEOS's ability to take advantage of high-performance computing capacities to model hydraulic fracturing problems in high fidelity.

6. CONCLUSION

A fully coupled method for the simulation of hydraulically driven fracture has been implemented in GEOS, a platform for massively-parallel multi-physics simulations. The proposed approach applies the finite element method to the standard equations of static equilibrium to model solid material deformation, and the finite volume method to the mass conservation equations to model the flow of fluid in the fracture. In this work, the extension of fractures is governed by the assumptions of linear elastic fracture mechanics, where we have proposed a modification to the virtual crack closure technique to allow for the applicability to problems involving fluid driven fractures. In addition, we have described how the proposed method avoids many of the difficulties encountered when updating the resulting changes in mesh topology in a massively parallel environment. Finally, an implicit time integration method was implemented for the solution of the fully coupled system.

For the purpose of verification, simulations using the method have been compared with semi-analytical solutions for three well-known problem geometries. Specifically, simulations of the KGD plane strain problem, radial fracture problem, and PKN problem showed excellent correlation with the zero-toughness and zero-viscosity solutions provided in [29, 30], and [32], respectively. In addition, because the proposed method does not rely on any assumptions meant to decouple the effects of fluid viscosity dissipation and the dissipation related to fracture growth, it may be applied uniformly for all dissipation regimes – thereby allowing the fully coupled physics to dictate the system response. In addition to showing excellent agreement with the verification problems, the proposed method was also validated with a hydraulically driven fracture experiment in PMMA, presented in [33].

Finally, the proposed method was shown to have the ability to simulate practical problems on length and time scales pertinent to hydraulic fracturing operations. This capability has been demonstrated through a field-scale simulation of a hydraulic stimulation of a realistic field site that included a pre-existing fracture network, and a variable *in situ* stress field.

ACKNOWLEDGEMENTS

Support for this work was provided by the LLNL LDRD project 'Creating Optimal Fracture Networks' (11-SI-006). This work performed under the auspices of the U.S. Department of Energy by Lawrence Livermore National Laboratory under Contract DE-AC52-07NA27344. LLNL release number LLNL-JRNL-654315.

REFERENCES

1. Newell RG. The long-term outlook for natural gas, energy information administration, 2011.
2. Ground water protection council, ALL consulting, modern shale gas development in the United States: a primer, 2009 April 116.
3. Adachi J, Siebrits E, Peirce A, Desroches J. Computer simulation of hydraulic fractures. *International Journal of Rock Mechanics and Mining Sciences* 2007; **44**:739–757.
4. Boone TJ, Ingraffea AR. A numerical procedure for simulation of hydraulically-driven fracture propagation in poroelastic media. *International Journal for Numerical and Analytical Methods in Geomechanics* 1990; **14**(1):27–47.

DOI: 10.1002/nag

5. Secchi S, Schrefler BA. A method for 3-D hydraulic fracturing simulation. *International Journal of Fracture* 2012; **178**(1-2):245–258.
6. Secchi S, Simoni L, Schrefler BA. Mesh adaptation and transfer schemes for discrete fracture propagation in porous materials. *International Journal for Numerical and Analytical Methods in Geomechanics* 2007; **31**(2):331–345.
7. Mohammadnejad T, Khoei AR. An extended finite element method for hydraulic fracture propagation in deformable porous media with the cohesive crack model. *Finite Elements in Analysis and Design* 2013; **73**:77–95.
8. Khoei AR, Hirmand M, Vahab M, Bazargan M. An enriched FEM technique for modeling hydraulically driven cohesive fracture propagation in impermeable media with frictional natural faults: numerical and experimental investigations. *International Journal for Numerical Methods in Engineering* 2015; **104**(6):439–468.
9. Irzal F, Remmers JJC, Huyghe JM, de Borst R. A large deformation formulation for fluid flow in a progressively fracturing porous material. *Computer Methods in Applied Mechanics and Engineering* 2013; **256**:29–37.
10. Gupta P, Duarte CA. Simulation of non-planar three-dimensional hydraulic fracture propagation. *International Journal for Numerical and Analytical Methods in Geomechanics* 2014; **38**(13):1397–1430.
11. Rangarajan R, Chiaramonte MM, Hunsweck MJ, Shen Y, Lew AJ. Simulating curvilinear crack propagation in two dimensions with universal meshes. *International Journal for Numerical Methods in Engineering* 2015; **102**(3-4): 632–670.
12. Fu P, Johnson SM, Carrigan CR. An explicitly coupled hydro-geomechanical model for simulating hydraulic fracturing in arbitrary discrete fracture networks. *International Journal for Numerical and Analytical Methods in Geomechanics* 2013; **37**:2278–2300.
13. Settgast RR, Johnson SM. Simulation of hydraulic fracture networks in three dimensions. *Proceedings, 37th Workshop on Geothermal Reservoir Engineering*, Stanford University, Stanford, 2012; SGP–TR–194.
14. Settgast RR, Johnson SM, Fu P, Walsh S, White J. Simulation of hydraulic fracture networks in three dimensions utilizing massively parallel computing resources. *SPE Unconventional Resources Conference (UrTec)*, Society of Petroleum Engineers, Denver, 2014.
15. Johnson SM, Settgast RR, Fu P, Walsh Stuart. Microseismicity and geomechanics: modeling and comparisons. *SPE Unconventional Resources Conference (URTEC)*, SPE, Denver, 2014.
16. Walsh S, Settgast R, Johnson S. A laboratory and numerical study of chemo-mechanically mediated permeability evolution in the near-wellbore region. *46th Meeting of the American Rock Mechanics Association*, ARMA, Chicago, 2012.
17. Walsh SDC, Du Frane WL, Mason HE, Carroll SA. Permeability of wellbore-cement fractures following degradation by carbonated brine. *Rock Mechanics and Rock Engineering* 2013; **46**(3):455–464.
18. Fu P, Hao Y, Walsh SDC, Carrigan CR. Thermal drawdown-induced flow channeling in fractured geothermal reservoirs. *Rock Mechanics and Rock Engineering* 2015:1–24.
19. Hao Y, Fu P, Carrigan CR. Application of a dual-continuum model for simulation of fluid flow and heat transfer in fractured geothermal reservoirs. *Proceedings, 38th Workshop on Geothermal Reservoir Engineering, vol SGP-TR-198*, Stanford University, Stanford, California, 2013.
20. Walsh SDC, Carroll SA. Fracture-scale model of immiscible fluid flow. *Physical Review E* 2013; **87**(1):013012.
21. Howard G, Fast CR. Optimum fluid characteristics for fracture extension. *Drilling and Production Practices The American Petroleum Institute*, New York, 1957; 261–270.
22. Kruger R. Virtual crack closure technique: history, approach, and applications. *Applied Mechanics Reviews* 2004; **57**(2):109–143.
23. Banks-Sills Leslie. Update: application of the finite element method to linear elastic fracture mechanics. *Applied Mechanics Reviews* 2010; **63**(2):020803.
24. Erdogan F, Sih GC. On the crack extension in plates under plane loading and transverse shear. *Journal of Basic Engineering* 1963; **85**(4):519–527.
25. Settgast RR. Numerical modeling of 3-dimensional surface separation (dissertation), 2006.
26. Settgast RR, Rashid MM. Continuum coupled cohesive zone elements for analysis of fracture in solid bodies. *Engineering Fracture Mechanics* 2009; **76**(11):1614–1635.
27. Khristianovic S, Zheltov Y. Formation of vertical fractures by means of highly viscous fluids. *4th World Petroleum Congress* 1955; **2**:579–586.
28. Geertsma J, De Klerk F, Geerstma J, de Klerck F. A rapid method of predicting width and extent of hydraulically induced fractures. *Journal of Petroleum Technology* 1969; **21**(12):1571–1581.
29. Detournay E. Propagation regimes of fluid-driven fractures in impermeable rocks. *International Journal of Geomechanics* 2004; **4**(1):35–45.
30. Savitski A, Detournay E. Propagation of a penny-shaped fluid-driven fracture in an impermeable rock: asymptotic solutions. *International Journal of Solids and Structures* 2002; **39**:6311–6337.
31. Perkins TKK, Kern LRR. Widths of hydraulic fractures. *Journal of Petroleum Technology* 1961; **13**(9):937–949.
32. Nordgren RP. Propagation of a vertical hydraulic fracture. *Society of Petroleum Engineers Journal* 1972; **12**(4): 306–314.
33. Rubin MB. Experimental study of hydraulic fracturing in an impermeable material. *Journal of Energy Resources Technology* 1983; **105**(2):116–124.
34. Mack MG, Warpinski NR. Mechanics of hydraulic fracturing. In *Reservoir Stimulation*, (2nd edition), Economides MJ, Nolte KG (eds). Prentice Hall Inc.: Old Tappan, NJ, 1989; 6.1–6.48.

DOI: 10.1002/nag

35. Settgast RR, Izadi G, Hurt RS, Jo H, Johnson SM, Walsh SDC, Moos D, Ryerson F, Livermore L, Incorporated BH, Llc AN. Optimized cluster design in hydraulic fracture stimulation. *SPE Unconventional Resources Conference (UrTec)*, 2015.
36. Fu P, Cruz L, Moos D, Settgast RR, Ryerson FJ. Numerical investigation of a hydraulic fracture bypassing a natural fracture in 3D. *49th US Rock Mechanics/Geomechanics Symposium*, San Francisco, 2015.

DOI: 10.1002/nag